The role of nitride species in the gas-phase furfural hydrogenation activity of supported nickel catalysts

Carmen Pilar Jiménez-Gómez[1], Chiara Defilippi[2], Juan Antonio Cecilia[1,*], Ramón Moreno-Tost[1], Pedro Maireles-Torres[1],Cristina Giordano[2,*]

[1] Departamento de Química Inorgánica, Cristalografía y Mineralogía (Unidad Asociada al ICP-CSIC). Universidad de Málaga Campus de Teatinos, 29071 Málaga (Spain).

[2] School of Biological and Chemical Sciences, Chemistry Department Queen Mary University of London. Mile End Road, London E1 4NS, United Kingdom.

Email: J.A. Cecilia: jacecilia@uma.es, C. Giordano: c.giordano@qmul.ac.uk

Abstract

A series of C-rich nickel nitride nanoparticles supported on silica has been prepared by the urea glass route, with urea as nitrogen and carbon source, and characterized by different physico-chemical techniques. They consist of Ni_3N nanoparticles of 20-25 nm embedded into a carbonaceous matrix. These catalysts are much more active and stable than a nickel supported silica catalyst, which drastically deactivates. The supported Ni_3N catalyst, with a 10 wt.% Ni, maintained a furfural conversion higher than 80% after 5 h of time-on-stream, at 170 ºC, with a high WHSV of 6 h^{-1}. Complete initial furfural conversion values were observed at reaction temperatures varying from 170 to 230ºC, and the selectivity toward furan and furfuryl alcohol (decarbonylation and hydrogenation products, respectively) was tuned by varying this temperature. After the catalytic tests, XPS and XRD have demonstrated that nanoparticles are stable, although carbonaceous deposits were also detected.

Keywords: nickel nitride • furfuryl alcohol • hydrogenation • furfural • biorefinery

1. Introduction

Since the industrial revolution, a dramatic increase in energy has been demanding, mainly from fossil resources. However, these are not sustainable for future perspectives since their depletion is leading to the extraction of low-degree feedstocks, with a negative impact for the environment. Considering this scenario, the scientific community is searching and developing alternative energy source, renewable and environmentally friendly. Among them, biomass together with the biogenic wastes are the only energy sources able to replace the traditional fossil fuels, since it is feasible to use it for the production of energy, biofuels and value-added chemicals. Despite its high availability, the type of biomass must be rigorously selected since it could interfere with the food chain. One of the biomass source with greatest potential to obtain chemicals is the lignocellulosic biomass, formed by lignin (15-25%), hemicellulose (20-35%) and cellulose (40-50%). Generally, each fraction of lignocellulose is treated to obtain valuable products [1]. Hemicellulose is formed by polysaccharides (xylans), which can be fragmented by hydrolysis in their respective monomers, obtaining mainly xylose. This C5 monomers can be dehydrated to furfural (FUR) in the presence of an acid catalyst [2]. FUR is used the starting point for the synthesis of a wide range of chemicals [3]. The presence of an aldehyde group and an α,β-unsaturated furan ring confers it high reactivity, in such a way FUR can be involved in hydrogenation, oxidation, decarbonylation, dehydration, alkylation, opening-ring, among other reactions [3,4].

In the case of the hydrogenation reaction, the commercial catalysts used in the process is copper chromite [5,6]. In spite of the good catalytic results, copper chromite is prone to undergo deactivation, mainly in gas-phase processes [7]. On the other hand, the presence of Cr species in the active phase is generating great controversy due to its high toxicity. Considering these premises, much attention is focused to develop environmentally benign catalytic systems with high activity, selectivity and stability. In this sense, it has been reported in the literature the catalytic activity of different transition metals for FUR hydrogenation [3,8,9], although their selectivity pattern is directly related to the hydrogenating character of the active site, as well as the acid and/or basic properties of the catalyst. Thus, Cu-based catalysts, which displays a lower hydrogenation capacity, lead to 2-methylfuran (MF) and furfuryl alcohol (FOL) due to the interaction of the FUR with the metal site that takes place through the carbonyl group of the FUR molecule [10-16]. FOL can be used in the synthesis of polymers with excellent thermochemical

stability, as well as in the synthesis of vitamin C or lysine [8]. In the case of MF, it can be employed as fuel additive since it increases the octane index [8]. On the other hand, transition metals with higher hydrogenating capacity, like Ni, give rise to a larger spectrum of reaction products, since the Ni sites can interact with the carbonyl group or the furan ring, obtaining, besides FOL and MF, other products such as 2-methyltetrahydrofuran, furan, tetrahydrofuran, even the opening of the furan ring to form alkanes [10,17-23]. Pd-based catalysts have also been employed in the FUR hydrogenation, favoring the formation of furan as the main product, since metal Pd sites favor the decarbonylation sites [10,24-27].

In the case of Ni-based catalysts, earlier studies indicated that the use of catalysts with an acidity gives rise to a wide variety of products and a strong deactivation after short reaction times [10]. In order to minimize the deactivation and to tune the selectivity pattern, the hydrogenating capacity was diminished by the incorporation of Fe species in the catalytic system, avoiding the ring opening [18]. Other alternative is related to the modulation of the physicochemical properties of catalysts. Thus, several authors have synthesized hydrotalcites with high Ni^0 loading, after calcination and subsequent reduction later reduced [21,22]. The next challenge was the design of catalytic systems with lower Ni content. Thereby, Ni-based catalysts supported on basic materials, such as MgO or Mg-clay minerals, have shown an excellent catalytic behavior [19,20]. Another alternative to modify the catalytic behavior of Ni species is the incorporation of a heteroatom that can diminish the hydrogenating capacity of Ni species. Thus, the incorporation of phosphorous species to form a nickel phosphide phase (Ni_2P), where the $P^{\delta-}$ centers bears part of the electronic density of the Ni species. This fact has an important effect on the catalytic behavior, since the Ni_2P-based catalysts are more active and stable than metal Ni catalysts. Moreover, the modification of the electronic density of Ni sites has a strong influence on the selectivity pattern [28]. In the same way, the formation of their respective nickel borides, carbides and nitrides can also present great potential in hydrogenation reactions. Metal nitrides and carbides, in particular, have shown the further advantage to have a tunable selectivity, depending on the reaction conditions [29,30]. The advantage of the synthesis procedure followed for the generation and incorporation of nickel nitride nanoparticles into a commercial silica support lies in using the nontoxic and non-aggressive urea as nitrogen precursor. The role of urea consists of: i) its decomposition provides the nitrogen to form the metallic nitride, ii) Ni(II) species are

partially reduced to form the $Ni^{\delta+}$ present in the nickel nitride and iii) favors the development of N-rich carbon matrix, which allows the nucleation and growth of the nanoparticles but in a controlled way, also preventing their aggregation. Metallic nickel is known to be a good catalyst and especially for hydrogenation of different functional groups. In contrast, few published works report the catalytic activity of nickel nitride and about its reactivity in hydrogenation using H_2. Specifically, there is a paper where the catalytic activity of Ni_3N has been studied in the hydrogenation reaction [29].

In the present work, a series of supported nickel nitride based catalysts has been prepared by using the urea glass route and a commercial silica as support. These catalysts have been characterized by XRD, XPS, TEM and N_2 sorption, and evaluated in the gas-phase hydrogenation of furfural. Special emphasis has been put on the elucidation of the active phase involved in the catalytic process, by using these supported catalysts.

2. Experimental Section

2.1. Catalyst Preparation

The synthesis of the Ni-catalysts followed the preparation previously reported [29] and here adapted for the specific reaction. Briefly, nickel acetate (1 g, $Ni(ac)_2$, Sigma-Aldrich 98%) was mixed with approximately 2.5 mL of ethanol, followed by the addition of urea ($CO(NH_2)_2$, Sigma-Aldrich 99%) with a urea/metal molar ratio R=3. After ultrasonicating, a homogeneous green solution was obtained. The Ni-urea precursor was then mixed with SiO_2 nanoparticles (10-20 nm, Sigma-Aldrich 99.5%), varying the percentage between Ni-salt and SiO_2 in order to obtain a theoretical 2.5 to 30 wt. % Ni in the final catalyst, supposing a Ni_3N-C-SiO_2 composition. The solutions were thermally treated at either 350 or 450 ˚C for 3 h (heating rate 5˚C/min) under nitrogen flow to prepare $Ni_3N/C/SiO_2$ or Ni/SiO_2, respectively. The catalysts were labeled as $xNi_3N/C/SiO_2$, where x is the Ni weight percentage used in the synthesis step. The carbon present in catalysts comes from the urea decomposition. It has been reported that the initial viscous nickel acetate-urea gel decomposes during the thermal treatment in nitrogen, with the formation of cyano-type complexes intermediates, which evolve towards nickel nitride nanoparticles embedded in a carbonaceous matrix [29]. For comparison, pure Ni_3N without the addition of SiO_2 was also prepared and tested.

It is well-known that Ni-based catalysts exhibit a high hydrogenating activity [9], and for this reason, a $Ni_3N/C/SiO_2$ catalyst was compared with a Ni/SiO_2 with a similar Ni

loading (10 wt. %). In the case of nickel nitride, a hybrid Ni_3N-carbon composite is formed after thermal treatment in N_2 at 350 ºC. The crystalline nickel nitride nanoparticles are embedded in a carbon matrix, with sizes of around 25 nm. These homogeneous particles are surrounded by a graphitic shell, avoiding surface oxidation upon storage in air. This is corroborated by the surface chemical analysis obtained from XPS, which affords values of 40.1 mol% C, 5.9 mol% N and 15.5 mol% Ni, with a Ni/N atomic ratio of 2.6, slightly lower than the stoichiometric value (3) of the hexagonal Ni_3N phase. All of catalyst after reaction were preserved in a solvent to avoid contact with air and therefore its oxidation.

2.2. Characterization of the catalysts

Samples were characterized by X-ray diffraction in an X'Pert Pro MPD automated diffractometer (PAN analytical). The patterns were recorded in Bragg–Brentano reflection configuration by using a Ge (111) primary monochromator (Cu $K\alpha_1$) and an X'Celerator detector with a step size of 0.0178 (2θ) between 2θ = 10 and 70º with an equivalent counting time of 712 s per step. XRD patterns were analysed by the Rietveld method, by using X'Pert Highscore Plus version 4.0 software. The crystallite size (D) was calculated by using the Williamson–Hall equation, $B\cos\theta = (K\lambda / D) + (2\,\varepsilon \sin\theta)$, where θ is the Bragg angle, B is the full width at half-maximum (FWHM) of the XRD peak, K is the Scherrer constant, λ is the X-ray wavelength, and ε is the lattice strain [31].

Textural properties were evaluated from the N_2 adsorption–desorption isotherms at -196 ºC, as determined by an automatic ASAP 2020 system from Micromeritics. Before the measurements, samples were outgassed for 10 h at 200 ºC and 2.7 Pa. The surface areas were determined with the BET equation and a N_2 cross-section of 16.2 $Å^2$ [32]. The total pore volume was calculated from the adsorption isotherm at $P/P_0 = 0.996$, and the average pore size was determined by applying the Barrett–Joyner–Halenda (BJH) method to the desorption branch. The DFT method was employed to determine pore size distributions [33].

The carbon, nitrogen and oxygen content, before and after the catalytic test, were determined by elemental analysis with a LECO CHN 932 analyser.

The transmission electron micrographs (TEM) were obtained with a Philips CCCM 200 Supertwin DX4 high-resolution transmission microscope. Microanalysis was carried out with an EDX Super-X system provided with 4 X-ray detectors and an X-FEG beam.

The XPS spectra were obtained with a Physical Electronics PHI 5700 spectrometer equipped with a multichannel detector, a hemispherical electron analyser (model 80-365B) and a non-monochromatic Mg K_α radiation (300 W, 15 kV, 1253.6 eV) X-ray source. High-resolution spectra were recorded at 45º take-off angle by a concentric hemispherical analyser operating in the constant-pass energy mode at 29.35 eV with a 720 m diameter analysis area. Charge referencing was measured against silicon of the SiO_2 employed as support (Si 2p at a binding energy (BE) of 103.5 eV), since samples contain different types of carbon. The pressure in the analysis chamber was kept lower than 5×10^{-6} Pa. PHI ACCESS ESCA-V6.0 F software package was used for the acquisition and data analysis. A Shirley-type background was subtracted from the signals. All of the recorded spectra were fitted with Gaussian–Lorentzian curves in order to determine more accurately the binding energies of the different element core levels. All samples were stored in sealed vials with an inert solvent to avoid oxidation. The samples were prepared in a dry box under a N_2 flow and analysed directly without previous treatment, and the solvent was evaporated before the introduction of the samples into the analysis chamber. In order to evaluate a possible evolution on the surface of catalysts, depth profiling was carried out using a 4 keV Ar^+ bombardment at a current density of ~1.5 μA/cm^2 for 30 min.

2.3. Catalytic tests

The gas-phase hydrogenation of FUR was performed in a 1/4“ tubular quartz reactor; the pelletized catalyst (200-400 m) was placed at the centre of the reactor tube between two layers of glass beads and quartz wool. Before the catalytic tests, catalysts were pre-treated *in situ* under a H_2 flow (60 mL min^{-1}, Airgas, 99.99%) at 350 ºC for 30 min. After this step, the catalysts were cooled to the selected reaction temperature under a H_2 flow (10-60 mL min^{-1}). Once this temperature was reached, a flow (3.87 mL h^{-1}) of a FUR solution in cyclopentyl methyl ether (CPME) (10 vol. %) was injected continuously with a Gilson 307SC piston pump (model 10SC). CPME is an environmentally friendly solvent and has been used in different organic reactions; thus, it is a green co-solvent for the selective dehydration of lignocellulosic pentoses to FUR [34].

These liquid samples were kept in sealed vials and analysed subsequently by GC with a Shimadzu GC-14B instrument equipped with a flame ionization detector and a capillary

column (CP Wax 52 CB). The FUR conversion and selectivity were calculated and defined by Equations (1) and (2):

$$Conversion\ (\%) = \frac{mol\ of\ furfural\ converted}{mol\ of\ furfural\ fed}\ x\ 100 \qquad (1)$$

$$Selectivity\ (\%) = \frac{mol\ of\ the\ product}{mol\ of\ furfural\ converted}\ x\ 100 \qquad (2)$$

$$Yield\ (\%) = \frac{mol\ of\ the\ product}{mol\ of\ furfural\ fed}\ x\ 100 \qquad (3)$$

3. Results and discussion

In a first step, XRD investigation was performed on samples as-prepared, with and without the addition of SiO_2, and treated at different temperatures in inert atmosphere. XRD results are reported in Figure 1. The catalyst prepared at 350°C ($10Ni/SiO_2$) consists of Ni_3N (ICDD: 00-010-0280) with a small component of Ni^0 (ICDD: 03-065-0380), while the one prepared at 450°C ($10Ni/SiO_2$) is formed by Ni^0 [35]. Regardless of the addition of silica, XRD patterns of both catalysts reveal that crystalline nanoparticles of similar sizes, around 22 nm (Williamson-Hall method), have been formed in every case (Figure 1). The two series of diffraction peaks at 2θ (º): 44.5 (111) and 51.8 (200), and 39.2 (110), 41.7 (002), 44.6 (111) and 58.6 (112), nicely match those expected for cubic nickel and hexagonal Ni_3N phases, respectively. The broad band at ~22º is attributed to the amorphous silica support. In no cases, the presence of cubic NiO associated with an intense diffraction peak at 43.2º (200) was detected. In fact, the synthetic route provide a reducing atmosphere during nanoparticles formation, hindering the oxidation of Ni.

The elemental analysis of $10Ni_3N/C/SiO_2$ shows percentages of 1.57 wt. % C and 0.61 wt. % N, higher than those of $10Ni/SiO_2$ (0.67 wt. % C and 0.09 wt. % N) (Table 1). This is due to the thermal treatment performed at higher temperature (450 ºC), at which nickel

nitride converts into metallic nickel, with the concomitant elimination of more reduced carbon and nitrogen species [29]. In any case, both the activation temperature (350 ºC) and reaction temperature (170-230 ºC) are lower than that used in this thermal treatment (450 ºC), thus minimizing the decomposition of nickel nitride.

The XRD patterns of the catalyst prepared with different nickel nitride content show an increase in the diffraction peak intensity with the loading (Figure 2). The presence of metallic nickel was detected, as can be inferred from the appearance of the characteristic diffraction peak at 51.8º. This peak becomes more visible as the percentage of Ni raises.

Concerning particle sizes, as determined by the Williamson-Hall equation, nickel nitride nanoparticles present values between 16 and 22 nm in diameter, whereas metal nickel sizes range from 15 to 28 nm.

TEM/elemental mapping investigation was conducted in order to confirm nanoparticles size and the presence of nickel nitride species in the catalysts. The $10Ni_3N/C/SiO_2$ catalyst was observed, before and after the test (Figure 3). It can be observed the presence of pseudo-spherical silica particles, which are used to support the nickel nitride particles (spherical dark nanoparticles) on this surface.

Two different particle sizes can be observed, being the smallest ones of 12.5 nm and the largest ones of 25 nm. However, from TEM analysis it is not feasible to discern between nickel and nickel nitride particles. For this reason, an EDX analysis was carried out to evaluate the distribution of different elements. This evidences a homogenous distribution of both silicon and oxygen. Similarly, C and N seem to be well dispersed, whereas the bright region are more enriched in Ni. The largest nickel particles are not accompanied by an enrichment in nitrogen, so it is expected that these particles could be ascribed to metal nickel species, although the low percentage of N in nickel nitride (Ni/N stoichiometry of 3:1) could justify the lack of N-enriched regions. However, in the elemental mapping, it is observed that N is good dispersed, although it is not very gathered due to its own nature. Textural properties of catalysts have been determined from their adsorption-desorption isotherms at -196 ºC. The adsorption-desorption isotherms are Type II in the IUPAC classification, where the interparticle void volume generates the macroporosity responsible of this isotherm shape. Thus, the higher fraction of N_2 is adsorbed at high relative pressure. However, some microporosity was also detected by

applying the t-plot (Table 1). After the Ni_3N incorporation, the specific surface area gradually decreases, mainly due to the filling of micropores, as can be deduced from the decrease in the micropore surface and pore volume.

In order to elucidate the chemical composition of the catalyst surface, as well as the oxidation state of each element on the surface, XPS analysis was carried out. As the catalyst is formed by a carbonaceous matrix, instead of selecting adventitious carbon as a reference, charge referencing was measured against the silica of the support in the Si 2p region (103.4 eV).

In the case of the Ni 2p core level spectra (Figure 4A), it can be observed a higher presence of Ni species on the catalyst surface as the Ni_3N loading increases, reaching the highest content in the case of $20Ni_3N/C/SiO_2$. The incorporation of larger amount of Ni species ($30Ni_3N/C/SiO_2$) does not enhance the surface Ni content, probably due to the formation of larger Ni nanoparticles, as suggested the intense X-ray diffraction peaks in the XRD discussion (Figure 2). Focusing on the Ni $2p_{3/2}$ region, it is noteworthy the presence of three peaks. The peak located at lower binding energy, about 852.0 eV, is ascribed to reduced Ni species [28,36]. However, this technique does not allow to discern between Ni^0 and $Ni^{\delta+}$ species coming from nickel carbide-nitride, since their binding energies overlap. Moreover, in all spectra, it can be observed a main peak located about 855 eV, attributed to unreduced Ni^{2+} species [28,36]. Considering that XRD patterns did not reveal any diffraction peaks ascribed to oxidized Ni species, we can assume that these Ni^2 species must present as an amorphous phase or formed by very small crystallites. As a further hypothesis, these Ni^{2+} species could also come from the re-oxidation of Ni^0 species after their contact with air. Finally, the band located about 861-862 eV could be ascribed to the shake-up satellite associated to Ni^{2+} species, being typical of divalent metal species [28,36].

In the case of the N 1s region (Figure 4B), the N content increases with the Ni_3N loading of catalysts. All catalysts display a single contribution located between 398.4-398.8 eV, ascribed to the overlapping of signals associated to C-N-C groups (398.9 eV) and carbon nitride species (398.1 eV) [37,38].

With regard to the C 1s core level spectra (Figure 4C), it can be observed that the C 1s contributions evolve according to the Ni_3N content. Thus, the catalysts with lower Ni_3N show a main contribution located about 282.9 eV, ascribed to carbide species, and a less

intense signal about 284.8 eV, attributed to the overlapping of signals associated to the adventitious carbon and the amorphous carbonaceous matrix. As the Ni_3N loading increases, the carbon in the form of carbide decreases such that the $30Ni_3N/C/SiO_2$ and Ni_3N bulk lack of this contribution while the adventitious carbon increases gradually. In addition, other less intense peaks located at 286.8 are observed, which could be in agreement with the formation of a N-rich carbon matrix (-C-N-C-) [37,39], while the contribution located about 288.8 is assigned to -C=O species, which could be associated to carbonate species resulting from urea decomposition. Finally, the O 1s region shows a single band about 532.8 eV, which is ascribed to the oxide species in the form of SiO_2. However, it is also noteworthy the presence of a band in the same binding energy for the Ni_3N bulk, attributable to oxygen-species coming from the urea thermal treatment, so it is not easy to discern between both contributions in the case of $Ni_3N/C/SiO_2$ catalysts.

As the Ni and Ni_3N-based catalysts display a high proportion of unreduced species, prior the tests, all catalysts were activated at 350 ºC in H_2 for 30 minutes to increase the contribution of Ni^0 or $Ni^{\delta+}$ species (Figure 5).

Ni 2p core level profiles (Figure 5) reveal an increase of the metallic or pseudo-metallic contribution. In addition, it is noticeable a decrease in the carbon and nitrogen content in the case of Ni_3N-based catalysts.

In order to elucidate the possible surface oxidation of Ni_3N catalysts during handling, the bulk Ni_3N undergone to an Ar^+-sputtering and, then, this sample was again analyzed by XPS (Figure 6). The Ni 2p core level spectrum of the fresh bulk Ni_3N displays a different profile than that shown after sputtering, since the contribution ascribed to Ni^{2+} species, about 855.5 eV, disappears while the band ascribed to Ni^0 or $Ni^{\delta+}$ (852.6 eV) increases. This fact suggests a partial oxidation of Ni species in the form of Ni_3N on the catalyst surface, probably due to its contact with the air. It is also feasible that this surface oxidized layer prevents oxidation of Ni_3N species. In the case of the C 1s core level spectrum, it can also be observed a change in the XPS profile, since a new contribution located about 283.2 eV appears. This contribution is assigned to the presence of carbide species, in such a way that the Ar^+ sputtering reveals that the carbide species are also prone to oxidation with the air contact. In summary, the Ar^+ sputtering study could point out the existence of a C-rich Ni nitride phase, which is difficult to detect by XRD. Finally, in the case of the N 1s core level spectrum, changes are hardly observed between the sample before and after the Ar^+ sputtering. From these data, it can be inferred that nitride species are more

stable under oxidizing conditions, while reduced carbon species are more likely to be oxidized.

4. Catalytic results

The $Ni_3N/C/SiO_2$ catalysts were evaluated in the gas-phase furfural hydrogenation. In a preliminary step, $10Ni_3N/C/SiO_2$ catalyst was selected to determine the reactivity of the cyclopentyl methyl ether as solvent under similar catalytic conditions than those studied in the furfural hydrogenation reaction below. The obtained results discarded the formation of reaction products, confirming this solvent is inert under the reaction conditions studied. Then, the catalytic performance of 75 mg bulk Ni_3N nanoparticles was evaluated, obtaining a negligible furfural conversion, probably due to the low amount of available active sites as a consequence of a very low specific surface area (5 m^2/g) exhibited by the Ni_3N nanoparticles [29]. This result has prompted the preparation of supported catalysts for a better nanoparticles dispersion and have the active phase in close contact with the support surface, whose interaction can provide stability and an enhancement of the catalytic activity associated to electronic modification could also be feasible. In the present work, a commercial silica [40] was used to support the Ni_3N nanoparticles. Similarly, commercial silica support does not possess active sites to catalyze the gas-phase hydrogenation of furfural. In the first catalytic study with supported Ni_3N catalysts, the influence of the catalyst loading was studied by varying the loading between 38 and 150 mg, by diluting with SiC to maintain the same height bed in the reactor, in order to determine the minimum amount of catalyst necessary to achieve the best catalytic performance. Only differences were found between the two lowest loadings (Figure 7).

The use of the highest amount of catalyst (150 mg of $10Ni_3N/C/SiO_2$ not shown) gives rise to full furfural conversion until 5 h of TOS at 210ºC, whereas with a half loading (75 mg) very close values were reached, with a FUR conversion after 5 h of TOS higher than 90%. However, with the lowest loading (38 mg) a lower catalytic activity is observed. This allows us to conclude that 75 mg of catalyst, diluted with SiC, is enough to attain a suitable catalytic performance. As regards the selectivity, the pattern does not seem to be related to the mass of catalyst, and, in particular, to the amount of active centers involved in the FUR hydrogenation. In all cases, it can be detected FOL and F as main products, while MF appears as minor product. According to the literature, this pattern suggest that there are two active sites involved in the reaction: decarbonylation sites for F formation and hydrogenation/hydrogenolysis sites for FOL and MF [20,22,28].

In this sense, the acyl interaction with the carbonyl group of furfural (μ^1-(O)-aldehyde bond) favors decarbonylation to furan. Moreover, a μ^2-(C,O) interaction has been justified by the repulsion occurring between monometallic Ni(111) surfaces and the furan ring, due to the overlap of the 3d band of surface metal atoms and the aromatic ring. In Scheme 1, the pathways leading to the reaction products are displayed. In the present work, the active sites are associated to the quasimetallic C-rich Ni nitride particles.

As the reaction takes place at the same temperature, the ratio (FOL+MF)/F is similar in all cases. Another parameter that should modify the selectivity pattern is the acid/base properties of the catalyst. Thus, the hydrogenolysis FOL → MF can be favored by the presence of acid sites. In this sense, the presence of unreduced Ni^{2+} species can provide Lewis acidity to the catalyst, which can favor the formation of MF. In fact, the amount of acid sites increases with the mass of catalyst (75 mg) and the selectivity to MF is higher (Y_{MF}: 24%) than FOL (Y_{FOL}: 8%), after 5 h of TOS at 210 ºC. On the contrary, with a lower proportion of acid sites (38 mg), the hydrogenolysis is not so favored, since, under similar catalytic conditions, the FOL yield is slightly higher than that of MF.

In the next study, the influence of the FUR fed was evaluated (Figure 8). As was expected, the increase in the FUR fed caused a decrease in FUR conversion, although considering the low amount of catalyst and FUR fed used, $10Ni_3N/C/SiO_2$ catalyst displays an excellent catalytic behavior in comparison to other catalysts tested under similar experimental conditions [12]. With regard to the selectivity, a clear change in the selectivity pattern can be observed, since a lower FUR fed (5 wt. %) favors the hydrogenolysis of FOL to form MF (Scheme 1). A higher FUR concentration increases the concurrence for active sites responsible of the consecutive hydrogenation-hydrogenolysis processes (Scheme 1: FUR → FOL → MF), in such a way that FOL molecules are replaced by FUR molecules before hydrogenolysis reaction takes place, as can be inferred from the increase in FOL yield and the concomitant decrease in MF formation. So it might be thought that the active centers of FUR hydrogenation are also those responsible of FOL hydrogenolysis.

Simultaneously, the decarbonylation process is slightly disfavoured when the FUR fed increases, as could be inferred from the decrease in furan yield. It must be considered that the active sites where MF is formed are more susceptible to deactivation, as the formation of water can affect active sites, due to oxidation and sintering processes. Moreover,

hydrogenolysis and decarbonylation are favoured at high reaction temperatures, as observed for low FUR concentration.

These data can be related with those indicated previously in the catalyst loading study, shown in Figure 7. As summary, it seems clear that the use of a lower proportion of furfural or higher mass of catalyst would enhance the interaction of FOL molecules with the available acid sites (Ni^{2+} species), which can favor the hydrogenolysis of FOL to MF. Thereby, for the test with higher FUR content (10 wt.%), as the amount of FUR molecules available per acid site is higher, the trend to form FOL as main product is more favorable.

On the other hand, $10Ni/SiO_2$ and $10Ni_3N/C/SiO_2$ were compared (Figure 9) to evaluate the role of the C-rich nitride species in the catalytic behavior. Concerning the catalytic performance, both catalysts, extrapolating to zero time, show full furfural conversion and similar selectivity values, being furan and furfuryl alcohol the main reaction products (Figure 9), but different stability was observed.

After 5 h of time-on-stream (TOS) at 210 ºC, the furfural conversion with $10Ni/SiO_2$ has drastically decreased, with a value lower than 40%, whereas the $10Ni_3N/C/SiO_2$ catalyst still maintains a conversion higher than 80%, probably due to the formation of a hybrid Ni_3N-carbon. As regards the selectivity pattern, in both cases, initially follows the trend: furan > furfuryl alcohol > 2-methylfuran, but along the TOS the decarbonylation activity seems to be lost, as can be inferred from the decrease in furan yield. This behavior could be explained by considering that the μ^1-acyl interaction is initially favored, although is prone to suffer deactivation along the TOS, whereas the μ^2-(C,O)-furfural interaction is maintained for longer reaction times [16].

The incorporation of a N-rich carbon matrix, where nickel nitride nanoparticles are embedded, does not modify the selectivity pattern; although, the amount of available metals on the surface as well as the hydrogenating capacity should be modified. For both catalysts, MF yield is below 10%, so the hydrogenolysis reaction of FOL to MF is disfavored under these experimental conditions [41]. These data suggest that both catalysts do not have enough acid sites (unreduced Ni^{2+} species or SiO_2) to favor the hydrogenolysis reaction. The obtained data differ with those reported for Ni_2P/SiO_2 catalysts under similar experimental conditions, where the main products were furan and MF [27]. The formation of MF was ascribed to the presence of unreduced phosphate species in the Ni_2P/SiO_2 catalyst, which provide Brönsted acid sites, thus promoting the

hydrogenolysis of FOL to MF. However, the presence of these acid sites made these catalysts more prone to deactivation along the TOS in comparison to the $Ni_3N/C/SiO_2$ catalysts.

After the tests, both $10Ni/SiO_2$ and $10Ni_3N/C/SiO_2$ catalysts were recovered and then analyzed by XPS. From the analysis of the Ni 2p core level spectra (Figure 5 and Table 2), it can be observed that the surface Ni content of $10N/SiO_2$ catalyst has diminished. In addition, the Ni^0 contribution increases in comparison to the fresh catalyst, while the amount of surface carbon suffers a substantial increase after the catalytic test. This fact seems to indicate that the deactivation of $10Ni/SiO_2$ catalyst is not due to the oxidation of Ni^0 sites to Ni^{2+}, but rather to the formation of carbonaceous deposits on its surface, which block the active sites involved in the FUR hydrogenation.

In the case of $10Ni_3N/C/SiO_2$ catalyst, strikingly, the surface Ni content raises after the catalytic test, although, contrary to the Ni/SiO_2 catalyst, the Ni^0 contribution (Figure 5) is not enhanced along the catalytic test. The surface carbon content also increases after the catalytic test, although this rise is much lower than that shown for the used Ni/SiO_2 catalyst. In addition, the N 1s spectra reveal that the intensity of typical band of the nitride species even increases after the catalytic test. This increase could be ascribed to the partial decomposition of carbide species, while the nitride species are more stable and resistant, as was inferred previously from the XPS data (Figure 6).

On the other hand, the C 1s core level spectra (Figure 5C) also present a clear evolution in this profile along the FUR hydrogenation reaction. These XPS data indicate that the carbide contribution disappears along the reaction, while the C-C carbon (284.8 eV) and the C-O contribution (287 eV) concomitantly increase, maybe as a consequence of the strong interaction of FUR molecules with surface active sites. The data of the C 1s core level spectra could suggest that nitride species are stable during the FUR hydrogenation process, while carbide species become very unstable, decomposing during activation and catalytic reaction. The stability of the Ni_3N phase is such that there are no important differences in the surface Ni/N molar ratio between the fresh and used catalysts.

Taking into account both the catalytic activity and XPS data, it is demonstrated that the $10Ni/SiO_2$ catalyst initially displays a higher proportion of surface Ni^0 species, which interact more strongly than Ni_3N with furfural molecules. In this sense, nitride species could modify the electronic density of Ni sites, in such a way that this interaction is

weakened. This fact means that the furfural can be more easily desorbed as indicated by the presence of a smaller amount of carbonaceous deposits on the catalyst surface, leading to more stable catalysts along TOS as a result of a greater availability of active sites.

The excellent catalytic performance of the supported Ni_3N catalyst led us to vary the nickel nitride loading incorporated to the silica to evaluate its influence on the catalytic performance. Thus, $Ni_3N/C/SiO_2$ catalysts with nominal Ni percentages between 2.5 and 30 wt. % were prepared, although the Ni loading must be lower than the theoretical values due to the presence of reduced carbon coming from the urea decomposition.

The catalytic data reveal that this family of catalysts display high stability along TOS, obtaining FUR conversion higher than 60 % after 5 h of TOS at 210 ºC, even for the catalyst with the lowest Ni_3N loading ($2.5Ni_3N/C/SiO_2$) (Figure 10a). In order to determine the optimum Ni_3N content, the reaction temperature was decreased until 170 ºC (Figure 10b). It must be taken into account that the lower reaction temperature is limited by the boiling point of FUR (161.7 ºC). At this lower reaction temperature, differences in catalytic performance as a function of the Ni loading are more important, although all catalysts maintain a high stability along the TOS. The catalytic data reveal that $10Ni_3N$-C-SiO_2 catalyst is the most active, although that with only 5 wt. % of Ni ($5Ni_3N/C/SiO_2$ catalyst) also displays a suitable stability. It is striking that the use of a larger amount of Ni content in the Ni_3N-based catalyst worsens the catalytic conversion, probably due to the agglomeration of particles, causing a decrease in the available Ni_3N involved in the FUR hydrogenation reaction. On the other hand, XRD data reveal that the catalysts with higher Ni content also display a higher proportion of Ni^0 species, which interaction with FUR molecules is stronger, thus favouring the formation of carbonaceous deposits, and consequently the catalyst deactivates. It could exist a relationship between catalytic activity and the presence of surface reduced carbon species, in such a way that catalysts with a higher amount of these species seem to be more active, mainly at lower reaction temperature.

As regards the selectivity pattern (Figure 10c-d), all catalysts display similar order (FOL > Furan > MF). It is noteworthy that the carbon balance is higher than 90 mol% in all cases, being only detected FOL, furan and MF as products, confirming that the reaction only proceeds by the interaction with the aromatic ring or the carbonyl group as was indicated previously (Scheme 1) [3], discarding the existence of undesired reactions. This product pattern differs from those reported in the earlier studies of Ni/SiO_2 in gas-phase

hydrogenation of FUR, where uncontrolled reaction as the hydrogenation of the carbonyl group and the furanic ring, as well as the decarbonylation and opening reaction were observed due to the interaction of Ni sites with both the aromatic ring and carbonyl group, although higher reaction temperatures than those reported in the present work were used [10]. More recently, other authors have synthesized NiMgAl and NiCoAl hydrotalcites, which were calcined and then reduced, obtaining high furfural conversions with furfuryl alcohol, methylfuran, tetrahydrofuran and furan as main products [21,22].

From these data, it could be inferred that the use of reaction temperatures above 230 ºC has an adverse effect in the selectivity pattern, since a wide range of products is detected, which, in turn, can generate carbonaceous deposits or other by-products (H_2O, CO, CO_2, small hydrocarbons) that can modify active sites. At the same time, a high catalytic activity can also cause a faster deactivation due to the cracking of FUR molecules generates carbonaceous deposits. The use of more severe reaction temperatures also favors furfural polymerization, mainly in the gas-phase reaction. This fact also generates carbonaceous deposits that interact strongly with the active centers, causing their fast deactivation. On the other hand, the acid/base support properties also have an important role in catalytic activity. Thus, the use of a basic support, such as MgO, favors the formation of FOL, furan and MF [20]; however, bifunctional acid-base supports (MgO-Al_2O_3) give rise to a wider range of products [10,28], while acid sites can even favor the opening of the furan ring [10]. The good catalytic performance of basic supports could be ascribed to a weaker interaction with the FUR. This more labile interaction favors an easier desorption of products, allowing a faster regeneration of the active site compared to those catalysts supported with higher acidity, which display a stronger interaction with the furan ring, or the carbonyl group, leading to uncontrolled reactions and FUR polymerization.

Regarding the reaction temperature (Figure 11), no influence on FUR conversion is observed, with values after 5 h of TOS ranging between 80 and 85%. However, the selectivity pattern is clearly modified depending. Thus the formation of FOL is favored at lower temperature, while the hydrogenolysis and decarbonylation processes become the main reaction pathways as temperature is increased [10,19]. In this sense, similar behaviour was observed for Ni/MgO catalysts, although working under less severe reaction conditions, only a WHSV of 1.5 h^{-1}, while in the present work the WHSV value is 6 h^{-1} [20]. Considering these data, it seems clear that FUR molecules tend to adopt the

μ^2-(C,O) conformation at lower temperature more easily [18]. However, the increase in the temperature favors the μ^1-acyl interaction, which is involved in the decarbonylation process. In addition, high temperatures also favor the formation of MF from FOL, through a hydrogenolysis reaction. As drawback, the increase in the temperature can also cause the formation of a higher proportion of carbonaceous deposits, as a consequence of the FUR polymerization.

As previously noted, the catalytic behaviour of this family of Ni_3N-based catalysts contrasts with that of nickel phosphide, Ni_2P, also supported on a commercial silica. In that case, at 190 ºC, a maximum conversion of 88 % was reached, with a yield of 2-methylfuran of 73 % for a catalyst with 15 wt.% of Ni [28]. The formation of FOL was hardly noticeable. This greater selectivity to MF was explained by the presence of Brönsted acid sites, associated with POH groups of non-reduced P species in the hydrogen phosphite form. However, a strong deactivation was observed due to the formation of carbonaceous deposits on the active sites, as demonstrated by XPS. In the case of the present work, the existence of weak acid sites on silica, as well as unreduced Ni^{2+} species, could justify that the hydrogenolysis reaction of FOL to MF is disfavored under the present experimental conditions.

Moreover, the influence of the H_2 flow on the catalytic behaviour was evaluated (Figure 12), which is directly related to the contact time of the FUR in the fixed bed reactor. The catalytic results show that an increase in the H_2 flow, that is, a low contact time, hardly decreases FUR conversion, although it is only noticeable for the test with a H_2 flow of 60 mL/min. The modification of the H_2 flow has a more pronounced effect on the selectivity pattern. The use of longer contact time (10 mL/min) leads to a quasi-equimolar ratio of F and FOL. The decrease in the contact time provokes a progressive decrease in F selectivity, from 44% (10 mL/min of H_2) to 17% (60 mL/min of H_2), which is accompanied by an increment of the FOL selectivity, from 45% to 70%, when the contact time increases. These data suggest that μ^1-(O)-aldehyde bond, which gives rise to the formation of F via decarbonylation reaction, is favored for longer contact time, whereas a decrease favors the μ^2-(C,O) interaction, thus leading to a higher amount of FOL. From these data, it can be inferred that μ^2-(C,O) interaction is stronger interaction than μ^1-(O)-aldehyde, although a higher temperature is required. This fact supposes that decarbonylation sites need to be regenerated longer time than hydrogenation sites, so the

use of longer contact time minimizes this strong interaction, in such a way that F selectivity increases.

After the catalytic tests at 170 ºC and 210 ºC, the used $10Ni_3N/C/SiO_2$ catalysts were recovered and analyzed by XRD, TEM and XPS.

XRD data reveal that the catalyst preserves the typical diffraction peaks of crystalline Ni^0 and Ni_3N phases (Figure 13), although the intensity of peaks located at 2θ: 37.3 and 39.1º decrease. This effect could be explained by the evolution of the Ni_3N species to Ni^0, the reduction of catalyst with H_2 before the test, or the amorphization of the nickel nitride phase.

The $10Ni_3N/C/SiO_2$ catalyst after the catalytic test at 210 °C was analyzed by TEM (Figure 3). The micrograph evidences particles of spherical morphology of Ni_3N, whose dimensions are preserved after the catalytic tests, according to XRD data (Figure 13). The EDX analysis shows that the dispersion of both C and N content hardly vary, so the catalytic process does not cause drastic modifications in the morphology and chemical composition of the $10Ni_3N/C/SiO_2$ catalyst.

The analysis of the surface chemical composition of the used catalyst was evaluated by XPS. Data displayed in Table 2 indicate the carbon on the surface raises after the catalytic test. This fact would confirm the formation of carbonaceous deposits, being more pronounced when the reaction temperature is higher (210 ºC), as a consequence of FUR polymerization, which is favored at high temperatures. In addition, it is striking that Ni content increases, whereas the N content is unchanged. From these data, it can be inferred that, in spite of the carbon deposition, the increase in the Ni content would suggest a partial decomposition of the C-N matrix, although the N content is maintained, so the decomposition of nitride species is very low or practically negligible.

In order to elucidate the mechanism of the FUR hydrogenation using $Ni_3N/C/SiO_2$, instead of FUR, the reaction was carried using FOL as fed (Figure 14). The conversion values are much lower than those reached when FUR was used, below 23% from the first hour of TOS. This low conversion could be explained by a weaker interaction of FOL with the active sites in comparison to FUR molecules. With regard to the yield, the furan is the main product obtaining a F yield of 11% after 1 h of TOS at 210 ºC, although this decrease with the reaction time, while MF increases slightly. From the catalytic data, it

can be deduced that the F is mainly obtained from the decarbonylation of FUR, although a small proportion of F could come from the decarbonylation of FOL.

The aim of the final study was to evaluate the role of the H_2 in the decarbonylation reaction (Figure 15). The results reveal that the use of an inert gas as He, instead of H_2, leads to a negligible conversion. From these data, it can be inferred that it is necessary a prior step where H_2 is homolytically cleaved to favor a subsequent decarbonylation via μ^1-(O)-aldehyde interaction.

5. Conclusions

The synthesis of silica-supported C-rich nickel nitride, by using the urea glass method, has allowed the preparation of a series of supported Ni_3N catalysts, with homogeneous particle sizes. These catalysts exhibit a high catalytic activity and stability in the gas-phase hydrogenation of furfural, being attained a furfural conversion higher than 80% after 5 h of TOS at 170 ºC, with a WHSV of 6 h^{-1} (four times higher than that reached in previous works), with the $Ni_3N/C/SiO_2$ catalyst with a 10 wt.% Ni. A Ni/SiO_2 catalyst, with a similar Ni content, showed a complete initial furfural conversion, but a quick deactivation was observed. The selectivity toward furan and furfuryl alcohol of the $Ni_3N/C/SiO_2$ catalyst (10 wt.% Ni) could be tuned by varying the reaction temperature, with complete furfural conversion between 170 and 230 ºC. XRD and XPS have demonstrated that used Ni_3N-based catalysts show similar structural and surface characteristics to the corresponding fresh catalysts, confirming that nickel nitride nanoparticles are stable, although the presence of carbonaceous deposits, due to the strong adsorption of FUR molecules on active sites, was also detected.

Acknowledgements

The authors are grateful to financial support from the Spanish Ministry of Innovation, Science and Universities (Project RTI2018-094918-B-C44) and FEDER (European Union) funds. J.A.C. thanks University of Malaga for contracts of PhD incorporation.

References

[1] S. G. Wettstein, D. Martin Alonso, E. I. Gürbüz, J. A. Dumesic. A roadmap for conversion of lignocellulosic biomass to chemicals and fuels. Curr. Opin. Chem. Eng. 1 (2012) 218-224.

[2] M. J. Climent, A. Corma, S. Iborra. Converting carbohydrates to bulk chemicals and fine chemicals over heterogeneous catalysts. Green Chem. 13 (2011) 520-540.

[3] R. Mariscal, P. Maireles-Torres, M. Ojeda, I. Sádaba, M. López Granados. Furfural: a renewable and versatile platform molecule for the synthesis of chemicals and fuels. Energy Environ. Sci. 9 (2016) 1144-1189.

[4] J. P. Lange, E. Van Der Heide, J. Van Buijtenen, R. Price. Furfural - a promising platform for lignocellulosic biofuels. ChemSusChem 5 (2012) 150-166.

[5] L. W. Burnett, I. B. Johns, R. F. Holdren, R. M. Hixon. Production of 2-methylfuran by vapor-phase hydrogenation of furfural. Ind. Eng. Chem. 40 (1948) 502-505.

[6] D. G. Manly, A. P. Dunlop. Catalytic hydrogenation. I. Kinetics and catalyst composition in the preparation of 2-methylfuran. J. Org. Chem. 23 (1958) 1093-1095.

[7] D. Liu, D. Zemlyanov, T. Wu, R. J. Lobo-Lapidus, J. A. Dumesic, J. T. Miller, C. L. Marshall. Deactivation mechanistic studies of copper chromite catalyst for selective hydrogenation of 2-furfuraldehyde. J. Catal. 299 (2013) 336-345.

[8] K. Yan, G. Wu, T. Lafleur, C. Jarvis. Production, properties and catalytic hydrogenation of furfural to fuel additives and value-added chemicals. Renew. Sustain. Energy Rev. 38 (2014) 663-676.

[9] S. Chen, R. Wojcieszak, F. Dumeignil, E. Marceau. How catalysts and experimental conditions determine the selective hydroconversion of furfural and 5-hydroxymethylfurfural. Chem. Rev. 118 (2018) 11023-11117.

[10] S. Sitthisa, D. E. Resasco. Hydrodeoxygenation of furfural over supported metal catalysts: A comparative study of Cu, Pd and Ni. Catal. Letters 141 (2011) 784-791.

[11] S. Sitthisa, T. Sooknoi, Y. G. Ma, P. B. Balbuena, D. E. Resasco. Kinetics and mechanism of hydrogenation of furfural on Cu/SiO_2 catalysts. J. Catal. 277 (2011) 1-13.

[12] C. P. Jiménez-Gómez, J. A. Cecilia, R. Moreno-Tost, P. Maireles-Torres. Selective production of 2-methylfuran by gas-phase hydrogenation of furfural on copper incorporated by complexation in mesoporous silica catalysts. ChemSusChem 10 (2017) 1448-1459.

[13] C. P. Jiménez-Gómez, J. A. Cecilia, I. Márquez-Rodríguez, R. Moreno-Tost, J. Santamaría-González, J. Mérida-Robles, P. Maireles-Torres. Gas-phase hydrogenation of furfural over Cu/CeO_2 catalysts. Catal. Today 279 (2017) 327-338.

[14] F. Dong, Y. Zhu, H. Zheng, Y. Zhu, X. Li, Y. Li. Cr-free Cu-catalysts for the selective hydrogenation of biomass-derived furfural to 2-methylfuran: The synergistic effect of metal and acid sites. J. Mol. Catal. A Chem. 398 (2015) 140-148.

[15] C.P. Jiménez-Gómez, J.A. Cecilia, F.I. Franco-Duro, M. Pozo, R. Moreno-Tost, P. Maireles-Torres. Promotion effect of Ce or Zn oxides for improving furfuryl alcohol yield in the furfural hydrogenation using inexpensive Cu-based catalysts. Mol. Catal. 455 (2018) 121-131.

[16] M.A. Jackson, M.G. White, R.T. Haasch, S.C. Peterson, J.A. Blackburn. Hydrogenation of furfural at the dynamic Cu surface of $CuOCeO_2/Al_2O_3$ in a vapor phase packed bed reactor. Mol. Catal. 445 (2018) 124-132.

[17] Y. Nakagawa, H. Nakazawa, H. Watanabe, K. Tomishige. Total hydrogenation of furfural over a silica-supported nickel catalyst prepared by the reduction of a nickel nitrate precursor. ChemCatChem 4 (2012) 1791-1797.

[18] S. Sitthisa, W. An, D. E. Resasco. Selective conversion of furfural to methylfuran over silica-supported Ni-Fe bimetallic catalysts. J. Catal. 284 (2011) 90-101.

[19] A. Guerrero-Torres, C. P. Jiménez-Gómez, J. A. Cecilia, C. García-Sancho, F. Franco, J. J. Quirante-Sánchez, P. Maireles-Torres. Ni supported on sepiolite catalysts for the hydrogenation of furfural to value-added chemicals: influence of the synthesis method on the catalytic performance. Top. Catal. 62 (2019) 535-550.

[20] C. P. Jiménez-Gómez, J. A. Cecilia, C. García-Sancho, R. Moreno-Tost, P. Maireles-Torres. Selective production of furan from gas-phase furfural decarbonylation on Ni-MgO catalysts. ACS Sustain. Chem. Eng. 7 (2019) 7676-7685.

[21] M. Manikandan, A. K. Venugopal, K. Prabu, R. K. Jha, R. Thirumalaiswamy. Role of surface synergistic effect on the performance of Ni-based hydrotalcite catalyst for highly efficient hydrogenation of furfural. J. Mol. Catal. A Chem. 417 (2016) 153-162.

[22] T. P. Sulmonetti, S. H. Pang, M. T. Claure, S. Lee, D. A. Cullen, P. K. Agrawal, C. W. Jones. Vapor phase hydrogenation of furfural over nickel mixed metal oxide catalysts derived from layered double hydroxides. Appl. Catal. A Gen. 517 (2016) 187-195.

[23] Z.X. Lia, X.Y. Wei, G.H. Liu, X.L. Meng, Z. Yang, S. Niu, D. Zhang, H.S. Gao, Z.H. Ma, Z.M. Zong. Highly selective hydrogenation of furfural and levulinic acid over $Ni_{0.09}Zn/NC_{600}$ derived from ZIFW-8. Mol. Catal. 480 (2020) 110651.

[24] M. Hronec, K. Fulajtarová. Selective transformation of furfural to cyclopentanone. Catal. Commun. 24 (2012) 100-104.

[25] S. Sitthisa, T. Pham, T. Prasomsri, T. Sooknoi, R. G. Mallinson, D. E. Resasco. Conversion of furfural and 2-methylpentanal on Pd/SiO_2 and $Pd-Cu/SiO_2$ catalysts. J. Catal. 280 (2011) 17-27.

[26] N. Pino, S. Sitthisa, Q. Tan, T. Souza, D. López, D. E. Resasco. Structure, activity, and selectivity of bimetallic $Pd-Fe/SiO_2$ and $Pd-Fe/\gamma-Al_2O_3$ catalysts for the conversion of furfural. J. Catal. 350 (2017) 30-40.

[27] L. Ruan, H. Zhang, M. Zhou, L. Zhu, A. Pei, J. Wang, K. Yang, C. Zhang, S. Xiao, B.H. Chen. A highly selective and efficient $Pd/Ni/Ni(OH)_2/C$ catalyst for furfural hydrogenation at low temperatures. Mol. Catal. 480 (2020) 110639.

[28] C. P. Jiménez-Gómez, J. A. Cecilia, R. Moreno-Tost, P. Maireles-Torres. Nickel phosphide/silica catalysts for the gas-phase hydrogenation of furfural to high-added-value chemicals. ChemCatChem 9 (2017) 2881-2889.

[29] G. Clavel, V. Molinari, A. Kraupner, C. Giordano. Easy access to Ni_3N– and Ni–carbon nanocomposite catalysts. Chem. - A Eur. J. 20 (2014) 9018-9023.

[30] A. Villa, S. Campisi, C. Giordano, K. Otte, L. Prati. Mo and W Carbide: Tunable catalysts for liquid phase conversion of alcohols. ACS Catal. 2 (2012) 1377-1380.

[31] G. K. Williamson, W. H. Hall. X-ray line broadening from filed aluminium and wolfram. Acta Metall. 1 (1953) 22-31.

[32] S. Brunauer, P. H. Emmett, E. Teller. Adsorption of gases in multimolecular layers J. Am. Chem. Soc. 60 (1938) 309-319.

[33] J. Landers, G. Y. Gor, A. V. Neimark. Density functional theory methods for characterization of porous materials. Colloids Surf. A 437 (2013) 3-32.

[34] C. P. Jiménez-Gómez, J. A. Cecilia, D. Durán-Martín, R. Moreno-Tost, J. Santamaría-González, J. Mérida-Robles, R. Mariscal, P. Maireles-Torres. Gas-phase hydrogenation of furfural to furfuryl alcohol over Cu/ZnO catalysts. J. Catal. 336 (2016) 107-115.

[35] C. Giordano, A. Kraupner, I. Fleischer, C. Henrich, G. Klingelhöfer, M. Antonietti. Non-conventional Fe_3C-based nanostructures. J. Mater. Chem. 21 (2011) 16963-16967.

[36] J. A. Cecilia, I. Jiménez-Morales, A. Infantes-Molina, E. Rodríguez-Castellón, A. Jiménez-López. Influence of the silica support on the activity of Ni and Ni_2P based catalysts in the hydrodechlorination of chlorobenzene. Study of factors governing catalyst deactivation. J. Mol. Catal. A Chem. 368 (2013) 78-87.

[37] A. Thomas, A. Fischer, F. Goettmann, M. Antonietti, J. O. Müller, R. Schlögl, J. M. Carlsson. Graphitic carbon nitride materials: variation of structure and morphology and their use as metal-free catalysts. J. Mater. Chem. 18 (2008) 4893-4908.

[38] A. N. Cloud, L. M. Davis, G. S. Girolami, J. R. Abelson. Low-temperature CVD of iron, cobalt, and nickel nitride thin films from bis[di(tert-butyl)amido]metal(II) precursors and ammonia. J. Vac. Sci. Technol. A Vacuum, Surfaces, Film. 32 (2014) 020606.

[39] M. Shalom, D. Ressnig, X. Yang, G. Clavel, T. P. Fellinger, M. Antonietti. Nickel nitride as an efficient electrocatalyst for water splitting. J. Mater. Chem. A 3 (2015) 8171-8177.

[40] B. A. T. Mehrabadi, S. Eskandari, U. Khan, R. D. White, J. R. Regalbuto, in *Adv. Catal.*, Elsevier Inc., **2017**, pp. 1–35.

[41] Y. Shi, Y. Zhu, Y. Yang, Y.-W. Y. W. Li, H. Jiao. Exploring furfural catalytic conversion on Cu(111) from computation. ACS Catal. 5 (2015) 4020-4032.

Table 1. Textural properties of catalysts

Sample	Textural properties			
	S_{BET} (m^2/g)	S_{micro} (m^2/g)	V_p (cm^3/g)	d_p (nm)
SiO_2	148.9	29.3	0.309	14.7
$2.5Ni_3N/C/SiO_2$	139.2	34.2	0.297	13.6
$5Ni_3N/C/SiO_2$	134.0	28.3	0.290	15.0
$10Ni_3N/C/SiO_2$	124.0	26.6	0.270	14.8
$20Ni_3N/C/SiO_2$	86.5	20.9	0.263	15.9
$30Ni_3N/C/SiO_2$	81.8	10.2	0.250	24.4
$10Ni/SiO_2$	127.0	29.5	0.273	15.3

Table 2. Surface chemical composition of the fresh and used catalyst determined by XPS.

	Atomic concentration (%)				
Catalyst	C	N	O	Si	Ni
$2.5Ni_3N/C/SiO_2$	19.51	0.32	52.67	26.79	0.71
$5Ni_3N/C/SiO_2$	18.67	0.34	52.86	27.51	0.62
$10Ni_3N/C/SiO_2$	16.07	0.45	53.59	26.79	1.10
$20Ni_3N/C/SiO_2$	14.78	2.57	52.86	24.19	5.60
$30Ni_3N/C/SiO_2$	10.43	1.53	57.10	27.42	3.52
$10Ni/SiO_2$ (with activ.)	6.14	-	61.20	31.81	0.86
$10Ni/SiO_2$ (after reaction)	20.25	-	52.62	26.71	0.43
$10Ni_3N/C/SiO_2$ (without activ.)	16.07	0.45	53.59	26.79	1.10
$10Ni_3N/C/SiO_2$ (with activ.)	13.80	0.29	56.60	28.30	1.01
$10Ni_3N/C/SiO_2$ (after reaction)	29.23	0.32	46.38	23.19	0.88

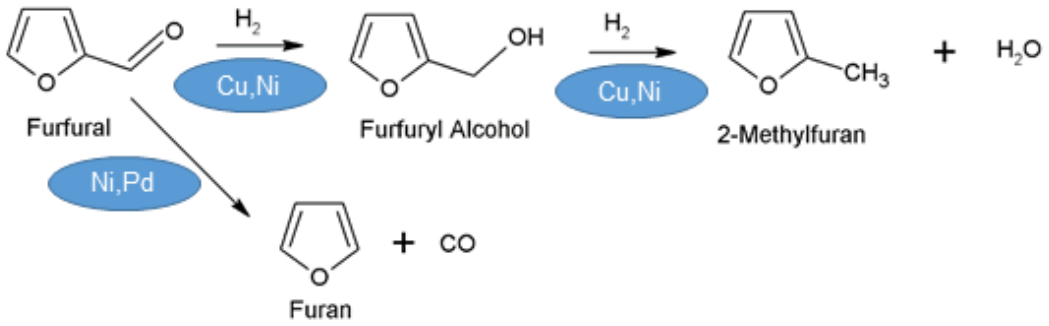

Scheme 1. Reaction pathways for hydrogenation and decarbonylation of furfural [3].

List of captions

Figure 1. XRD comparison of $10Ni/SiO_2$ and $10Ni_3N/C/SiO_2$ samples, obtained after treatment at 450 °C and 350 °C, respectively. Red and black vertical lines correspond to Ni_3N (ICDD: 00-010-0280) and Ni^0 (ICDD: 03-065-0380) databases.

Figure 2. XRD pattern of a) $2.5Ni_3N/C/SiO_2$, b) $5Ni_3N/C/SiO_2$, c) $10Ni_3N/C/SiO_2$, d) $20Ni_3N/C/SiO_2$ and e) $30Ni_3N/C/SiO_2$

Figure 3. TEM images of $10Ni_3N/C/SiO_2$ A) before and B) after the catalytic test at 210 °C and corresponding elemental mapping.

Figure 4. XPS spectra of A) Ni 2p, B) N 1s and C) C 1s of a) $2.5Ni_3N/C/SiO_2$, b) $5Ni_3N/C/SiO_2$, c) $10Ni_3N/C/SiO_2$, d) $20Ni_3N/C/SiO_2$, e) $30Ni_3N/C/SiO_2$ and f) bulk-Ni_3N.

Figure 5. XPS spectra of A) Ni 2p, B) N 1s and C) C 1s core level spectra of $10Ni/SiO_2$ (a,b,c) and $10Ni_3N/C/SiO_2$ (a',b',c'). (Raw catalyst (a), pre-treated catalyst under H_2 flow (b) and used catalyst (c)).

Figure 6. XPS spectra of A) Ni 2p, B) N 1s and C) C 1s of the bulk $10Ni_3N$ before and after the Ar^+-sputtering.

Figure 7. Catalytic performance for different loadings of $10Ni_3N/C/SiO_2$. (C: furfural conversion, F: furan, FOL: furfuryl alcohol, MF: 2-methylfuran; Experimental conditions: T= 210 ºC, H_2 flow= 10 mL min^{-1}, feed flow= 2.3 $mmol_{FUR}\ h^{-1}$).

Figure 8. Influence of the furfural feed on the catalytic performance of $10Ni_3N/C/SiO_2$ (Experimental conditions: m_{cat}= 75 mg, T= 210 ºC, TOS= 5 h, H_2 flow= 10 mL min^{-1}, feed flow values= 2.3 (5 vol%) and 4.6 (10 vol%) $mmol_{FUR}\ h^{-1}$)

Figure 9. Catalytic performance of Ni_3N- and Ni-based catalysts (10 wt% Ni) (Experimental conditions: m_{cat}= 75 mg, T= 210 ºC, H_2 flow= 10 mL min^{-1}, feed flow= 4.6 $mmol_{FUR}\ h^{-1}$)

Figure 10. Evolution of the catalytic performance as a function of the Ni_3N loading at a reaction temperature of (a) 210 ºC, (b, c and d) 170 ºC (Experimental conditions: m_{cat}= 75 mg, H_2 flow= 10 mL min^{-1}, feed flow= 4.6 $mmol_{FUR}\ h^{-1}$)

Figure 11. Influence of the reaction temperature on the catalytic performance of $10Ni_3N/C/SiO_2$ (Experimental conditions: m_{cat}= 75 mg, TOS= 5 h, H_2 flow= 10 mL min^{-1}, feed flow= 4.6 $mmol_{FUR}\ h^{-1}$)

Figure 12. Influence of H_2 flow on the catalytic performance of $10Ni_3N/C/SiO_2$ (Experimental conditions: m_{cat}= 75 mg, TOS= 5 h, T= 210 ºC, feed flow= 4.6 $mmol_{FUR}\ h^{-1}$)

Figure 13. XRD comparison of the $10Ni_3N/C/SiO_2$ sample, before and after the catalytic test

Figure 14. Catalytic activity of $10Ni_3N/C/SiO_2$ by feeding 10 vol% furfuryl alcohol (Experimental conditions: m_{cat}= 75 mg, TOS= 5 h, T= 210 ºC, H_2 flow= 10 mL min^{-1}, feed flow= 4.6 $mmol_{FOL}\ h^{-1}$)

Figure 15. Influence of the gas flow type (H_2 or He) on the catalytic performance of $10Ni_3N/C/SiO_2$ (Experimental conditions: m_{cat}= 75 mg, TOS= 5 h, T= 210 ºC, gas flow= 10 mL min^{-1}, feed flow= 4.6 $mmol_{FUR}\ h^{-1}$)

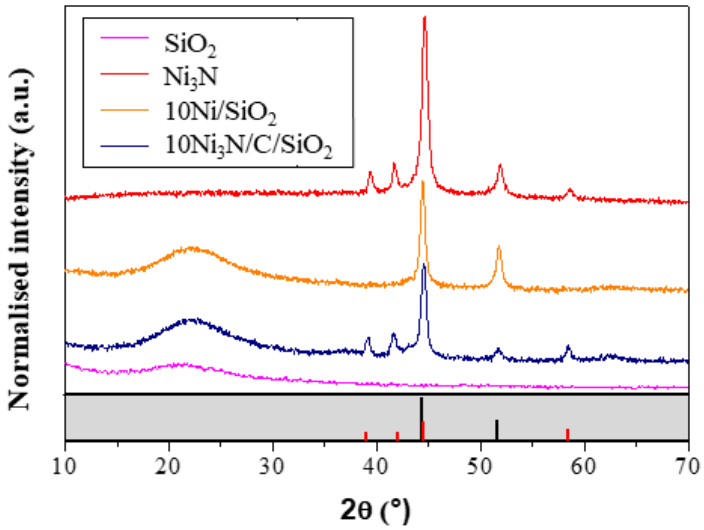
SiO2
Ni3N
10Ni/SiO2
10Ni3N/C/SiO2
Normalised intensity (a.u.)
10
20
30
40
50
60
70
2θ (°)

Figure 1

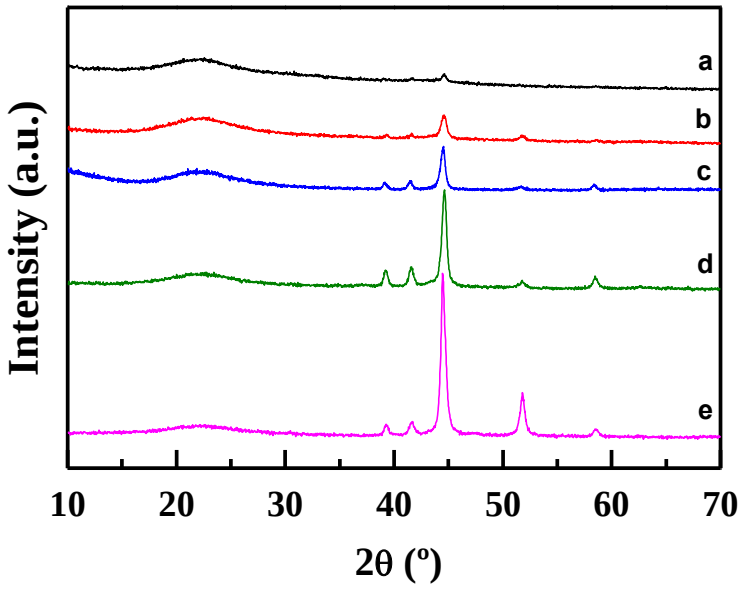

Figure 2

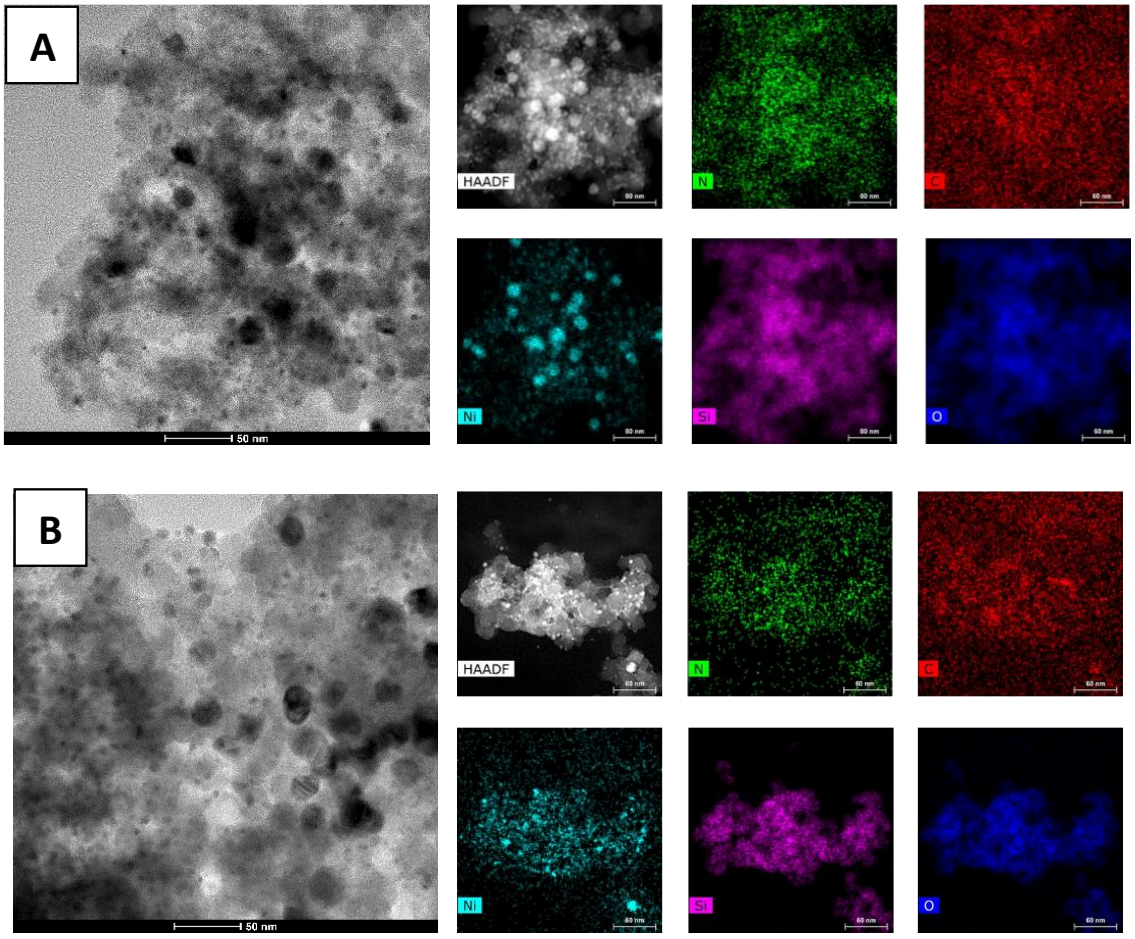

Figure 3

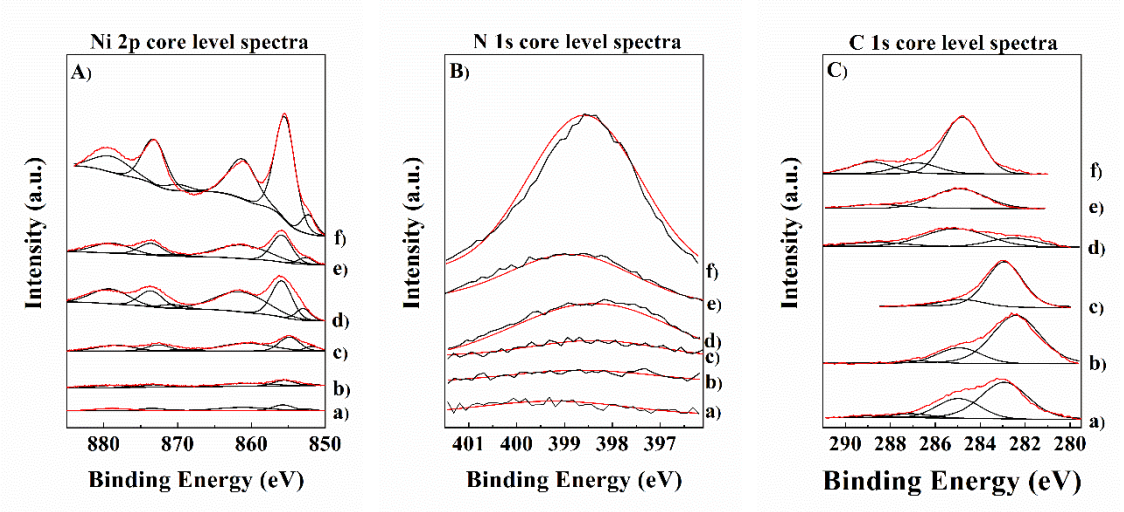
Ni 2p core level spectra
A)
Intensity (a.u.)
f)
e)
d)
c)
b)
a)
880
870
860
850
Binding Energy (eV)
N 1s core level spectra
B)
Intensity (a.u.)
f)
e)
d)
c)
b)
a)
401
400
399
398
397
Binding Energy (eV)
C 1s core level spectra
C)
Intensity (a.u.)
f)
e)
d)
c)
b)
a)
290
288
286
284
282
280
Binding Energy (eV)

Figure 4

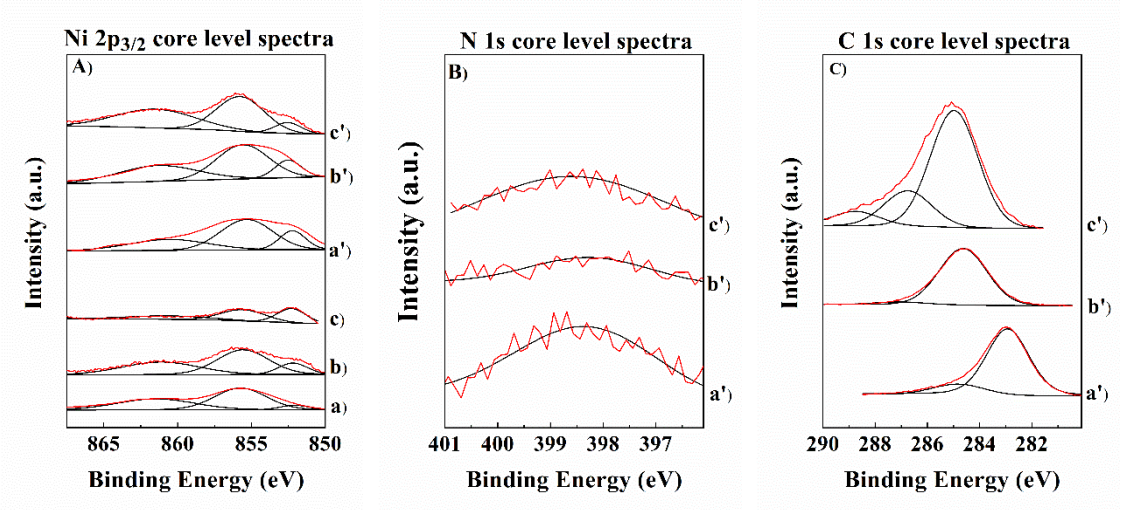
Ni 2p3/2 core level spectra
A)
Intensity (a.u.)
c')
b')
a')
c)
b)
a)
865
860
855
850
Binding Energy (eV)
N 1s core level spectra
B)
Intensity (a.u.)
c')
b')
a')
401
400
399
398
397
Binding Energy (eV)
C 1s core level spectra
C)
Intensity (a.u.)
c')
b')
a')
290
288
286
284
282
Binding Energy (eV)

Figure 5

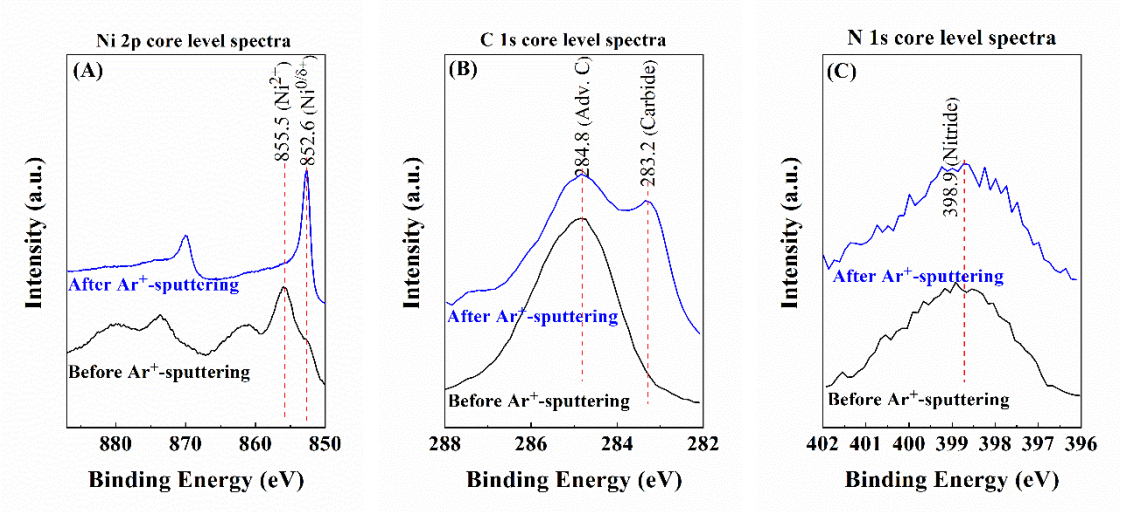
Ni 2p core level spectra
(A)
855.5 (Ni2−)
852.6 (Ni0/δ+)
After Ar+-sputtering
Before Ar+-sputtering
Intensity (a.u.)
880
870
860
850
Binding Energy (eV)
C 1s core level spectra
(B)
284.8 (Adv. C)
283.2 (Carbide)
After Ar+-sputtering
Before Ar+-sputtering
Intensity (a.u.)
288
286
284
282
Binding Energy (eV)
N 1s core level spectra
(C)
398.9 (Nitride)
After Ar+-sputtering
Before Ar+-sputtering
Intensity (a.u.)
402
401
400
399
398
397
396
Binding Energy (eV)

Figure 6

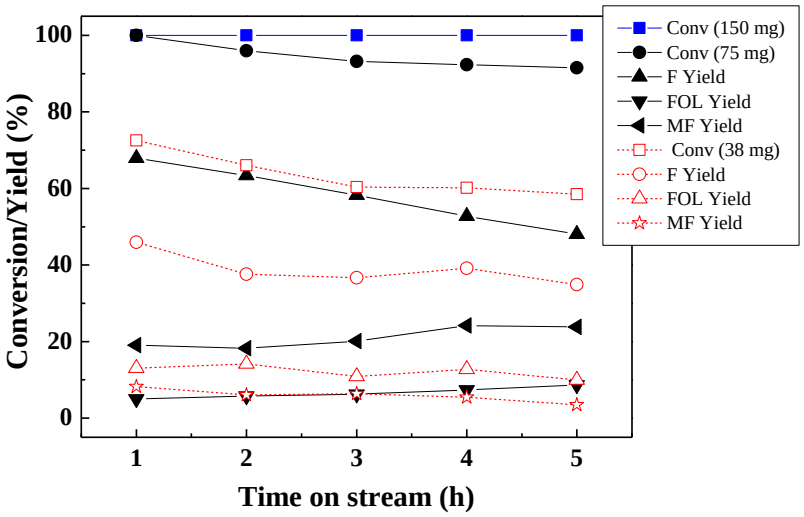
Conv (150 mg)
Conv (75 mg)
F Yield
FOL Yield
MF Yield
Conv (38 mg)
F Yield
FOL Yield
MF Yield
Conversion/Yield (%)
Time on stream (h)
0
20
40
60
80
100
1
2
3
4
5

Figure 7

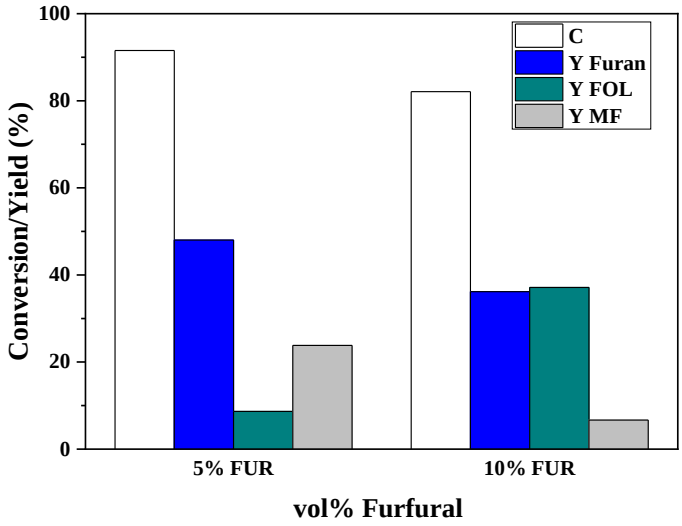
100
80
60
40
20
0
Conversion/Yield (%)
C
Y Furan
Y FOL
Y MF
5% FUR
10% FUR
vol% Furfural

Figure 8

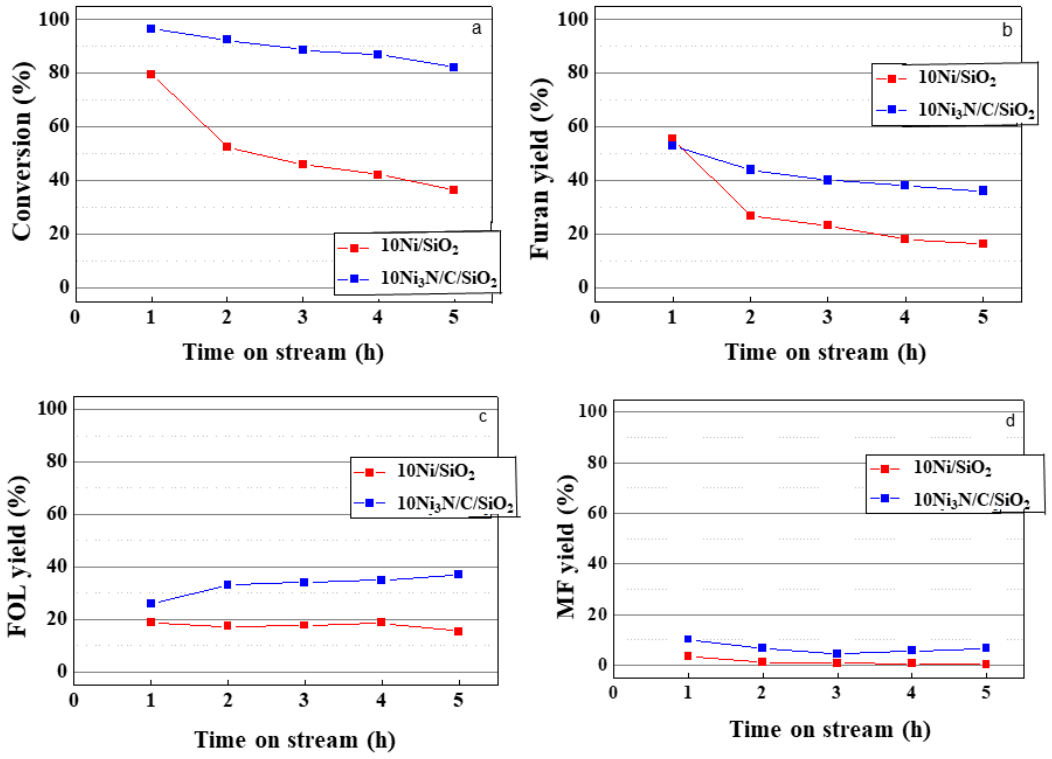
a
Conversion (%)
Time on stream (h)
10Ni/SiO2
10Ni3N/C/SiO2
b
Furan yield (%)
Time on stream (h)
10Ni/SiO2
10Ni3N/C/SiO2
c
FOL yield (%)
Time on stream (h)
10Ni/SiO2
10Ni3N/C/SiO2
d
MF yield (%)
Time on stream (h)
10Ni/SiO2
10Ni3N/C/SiO2

Figure 9

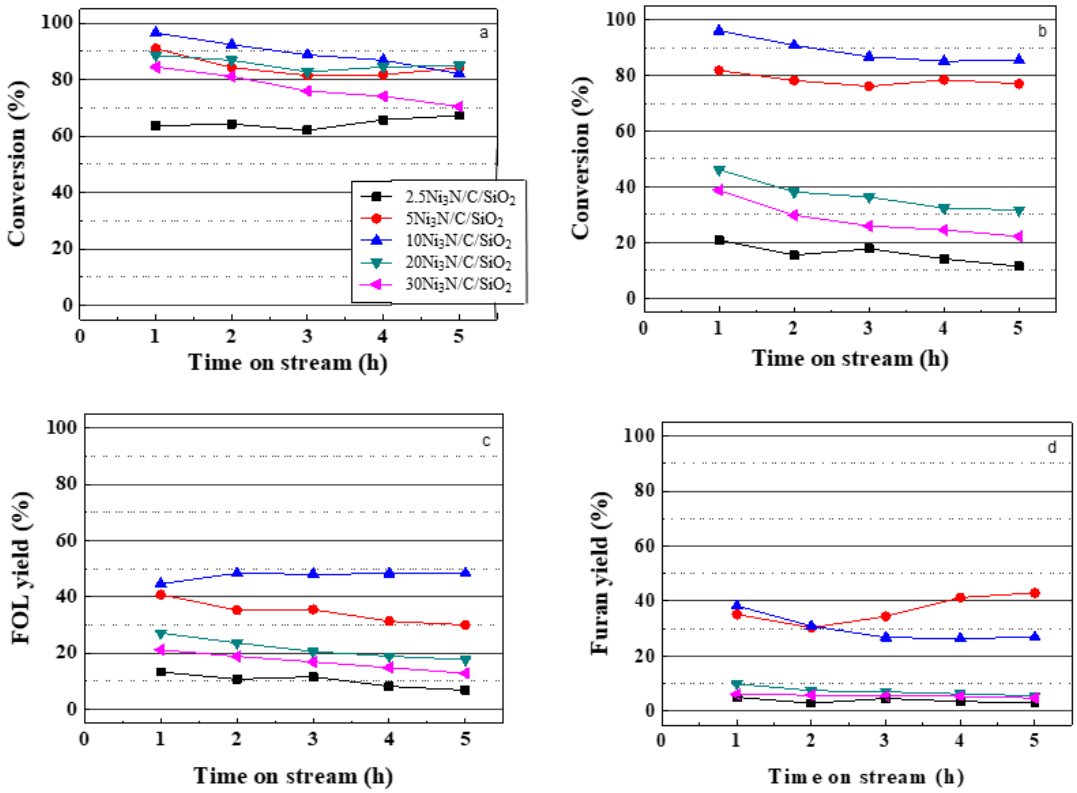
a
Conversion (%)
Time on stream (h)
2.5Ni3N/C/SiO2
5Ni3N/C/SiO2
10Ni3N/C/SiO2
20Ni3N/C/SiO2
30Ni3N/C/SiO2
b
Conversion (%)
Time on stream (h)
c
FOL yield (%)
Time on stream (h)
d
Furan yield (%)
Time on stream (h)

Figure 10

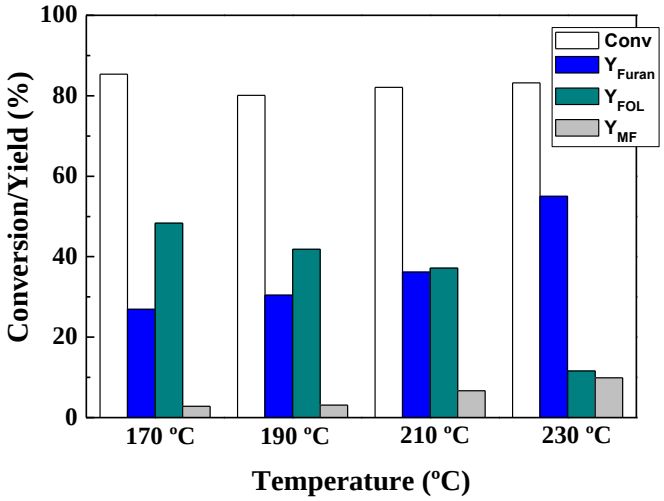
Conv
Y Furan
Y FOL
Y MF
Conversion/Yield (%)
100
80
60
40
20
0
170 °C
190 °C
210 °C
230 °C
Temperature (°C)

Figure 11

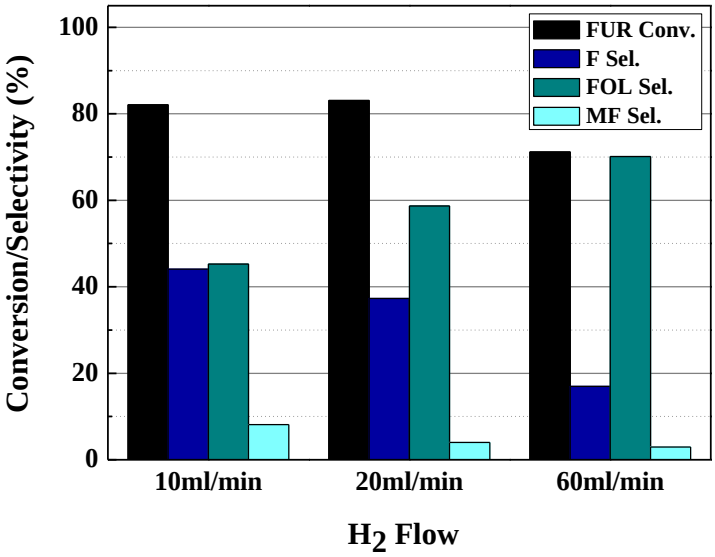
Conversion/Selectivity (%)
100
80
60
40
20
0
FUR Conv.
F Sel.
FOL Sel.
MF Sel.
10ml/min
20ml/min
60ml/min
H2 Flow

Figure 12

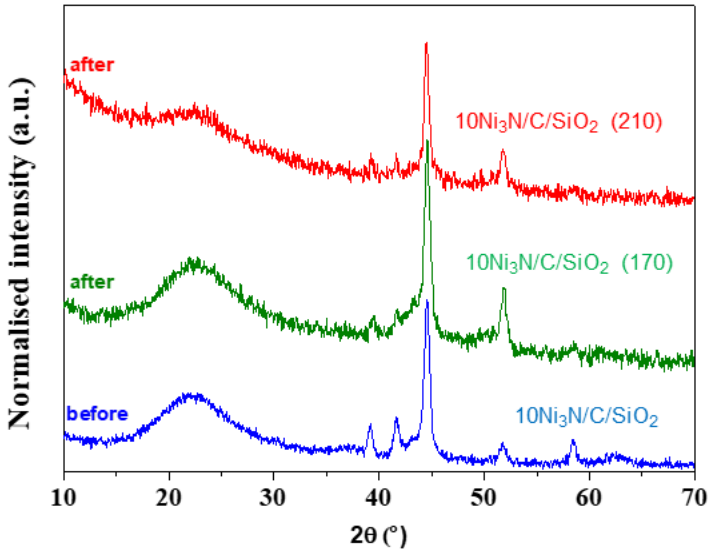
after
10Ni3N/C/SiO2 (210)
after
10Ni3N/C/SiO2 (170)
before
10Ni3N/C/SiO2
Normalised intensity (a.u.)
10
20
30
40
50
60
70
2θ (°)

Figure 13

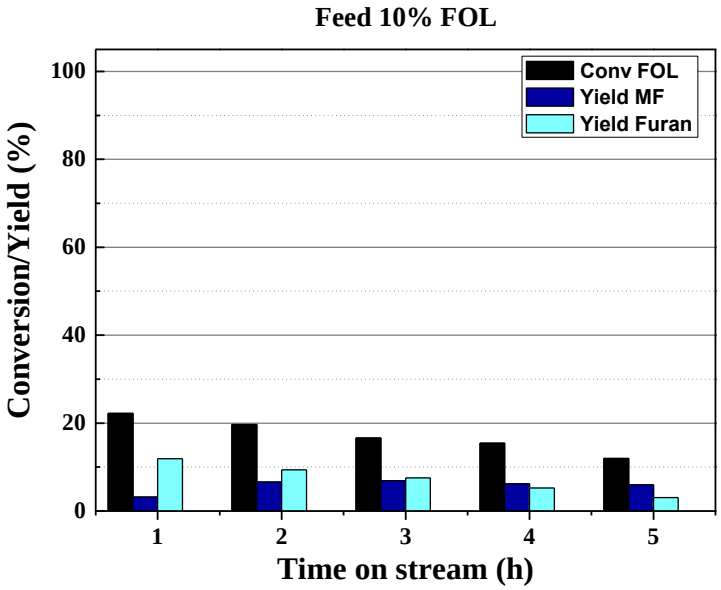
Feed 10% FOL
Conv FOL
Yield MF
Yield Furan
Conversion/Yield (%)
100
80
60
40
20
0
1
2
3
4
5
Time on stream (h)

Figure 14

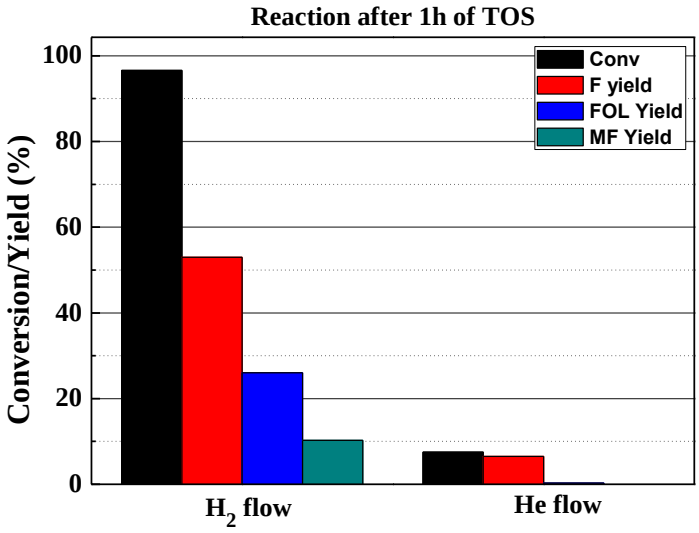
Reaction after 1h of TOS
Conversion/Yield (%)
100
80
60
40
20
0
Conv
F yield
FOL Yield
MF Yield
H2 flow
He flow

Figure 15